One dimensional wavefront sensor development for tomographic flow measurements[1]

D. Neal
Sandia National Laboratories, PO Box 5800, Albuquerque, NM 87185-0601

R. Pierson
E. Chen
K. Bishop
Applied Technology Associates, 1900 Randolph S.E., Albuquerque, NM 87106

L. McMackin
Air Force Phillips Laboratories, Kirtland AFB, NM 87117

ABSTRACT

Optical diagnostics are extremely useful in fluid mechanics because they generally have high inherent bandwidth, and are non-intrusive. However, since optical probe measurements inherently integrate all information along the optical path, it is often difficult to isolate out-of-plane components in 3-dimensional flow events. It is also hard to make independent measurements of internal flow structure. Using an arrangement of one-dimensional wavefront sensors, we have developed a system that uses tomographic reconstruction to make two-dimensional measurements in an arbitrary flow. These measurements provide complete information in a plane normal to the flow. We have applied this system to the subsonic free jet because of the wide range of flow scales available.

These measurements rely on the development of a series of one-dimensional wavefront sensors that are used to measure line-integral density variations in the flow of interest. These sensors have been constructed using linear CCD cameras and binary optics lenslet arrays. In designing these arrays, we have considered the coherent coupling between adjacent lenses and have made comparisons between theory and experimental noise measurements. This paper will present examples of the wavefront sensor development, line-integral measurements as a function of various experimental parameters, and sample tomographic reconstructions.

Keywords: Wavefront sensor, Binary optics, diffractive optics, optical diagnostics

1. INTRODUCTION

Optical diagnostics have long been applied to fluid dynamics measurement problems. They provide non-intrusive measurements of fluid parameters, often with good dynamic range and excellent sensitivity. Optical techniques have been used to measure all aspects of the fluid state including: temperature, pressure, velocity, density and species using a wide variety of techniques. However, there are relatively few techniques that can be used to look at the internal structure of a asymmetric or unsteady flow. Many of the techniques used to infer density (schlieren, interferometry, absorption, etc.) use an integrated line of sight. It isn't possible, without additional apriori information, to determine the internal structure of the flow. To overcome this problem, we have developed a tomographic system designed to deduce this structure.

In general, tomography is a method of combining the data from a set of line-of-sight integrated measurements to reconstruct, through mathematical inversion, the spatially resolved details of an object. In medical computed tomography (CT scans), a set of x-ray absorption measurements are combined to reconstruct the details of the internal organs in a slice of the body. For the fluid dynamics problem at hand, a set of optical phase measurements is to be used to reconstruct the details of density structure in a slice of a dynamic heated jet air flow.

[1] This work was supported by the United States Department of Energy under contract number DE-AC04-94L85000 and by AFOSR.

0-8194-1905-2/95/$6.00

To produce the necessary set of measurements, a number of lasers are arranged in a 180 degree arc around the flow. The expanded, collimated beams from these lasers propagate through the flow at different directions, intersecting at a common plane of the flow. One-dimensional (1D) linear sensor arrays (see Fig. 1) that are capable of measuring the phase of optical radiation after it has propagated through the flow field are arranged on the opposite side. These wavefront sensors, to be described in more detail in the following sections, measure the optical path errors induced on the laser beams by the density variations in the flow caused by the mixture of heated air and entrained cooler room air in the jet. Although each sensor array detects the path-integrated phase in a particular direction through the flow, the set of sensor arrays collects information along many different directions through the flow simultaneously, enabling the inversion of the data set and yielding a detailed spatially resolved picture of the plane of the flow through which all the lasers propagated. When the set of sensor arrays in this optical tomography system is operated at speeds of several kilohertz, a tomographic movie of the flow structure in a 2D plane of the flow can be obtained frame by frame[1].

The resolution of tomographic images that are reconstructed from these measurements depends on the number of sensors arranged around the flow as well as the spatial resolution of each sensor array. Extensive modeling of the characteristics of the Shack-Hartmann wavefront sensor arrays and the tomographic reconstruction algorithms are performed to determine the number of sensor arrays and the number of subapertures in each array that are necessary to capture sufficient detail in the flow reconstructions. The details of these simulations and comparison to experimental measurements are presented in Sections 2 and 3. The tomography system design is discussed in Section 4.

To use tomography to deduce the structure of a 3D, non-steady flow, an appropriate sensor must be selected. The sensor must have sufficient dynamic range to cope with the expected variations of the flow, have high bandwidth to resolve the time-dependence, and have adequate spatial resolution. Furthermore, it must be robust and low cost so that a number of sensors may be used simultaneously. Based on previous work[2], a one-dimensional wavefront sensor was selected as capable of meeting all these requirements. This sensor has excellent dynamic range, runs at several kHz, and has good sensitivity. It is constructed using precision binary optics and conventional linear CCD cameras.

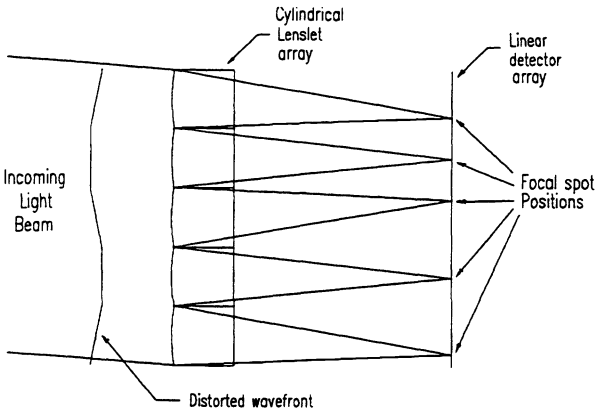

Figure 1 - Basic elements of wavefront sensor system. For the one-dimensional sensor the lenslet array is cylindrical and the detector is a line-scan camera array.

2. WAVEFRONT SENSOR DESIGN

The basic elements of the wavefront sensor are depicted in Figure 1. The sensor consists of a lenslet array, a detector array and data acquisition and analysis modules. Since the objective of this effort is the application of tomography to infer density distributions in a non-steady flow, high speed data acquisition is necessary. While various high speed framing cameras are available, the large number of views and the high cost associated with these cameras was considered prohibitive. Thus a one-dimensional wavefront sensor was selected. This will allow measurement of the density distribution in plane slice through the flow, and the plane location can be varied to infer the 3D distribution. We have fabricated several different lenslet arrays using binary optics technology, and use off-the-shelf CCD linear cameras for the detector elements. Data acquisition is performed either with a 12 bit A/D CAMAC-based transient digitizer, or with a VME-based 12 bit A/D. Data acquisition and basic analysis have been described in a previous paper[2].

2.1 Binary optics design

One of the key problems with the development of a Shack-Hartmann wavefront sensor is the fabrication of the lenslet array needed. In previous work, we have used discrete small cylindrical lenses to build several low resolution sensors. We also introduced the concept of using binary optics to fabricate these arrays. The binary optics technique has proven to be successful and is capable of making a large number of different devices with high fidelity.

The basic steps in fabricating a binary optic are depicted in Figure 2. The optical element desired is designed using

commercial mask layout software (DW-2000) and a set of custom macros that are used to design the lens. These designs are written with an e-beam system to make a set of four to six optical masks on high quality substrates. The mask pattern is then transferred to the desired substrate by coating the substrate with photo resist, exposing through the mask with ultraviolet light, and then developing the resulting pattern. This pattern is etched into the substrate (fused-silica in most cases) using reactive-ion etching. This process creates a single depth pattern over the desired aperture. To build up the desired surface profile, the process is repeated with a second mask layer, only it is etched to twice the depth of the first etch. This process then begins to approximate the curved surface of a typical lens element in a digital fashion. We usually repeat this process four times to build structures with sixteen different levels. A sixteen level structure (with total sag of 1 wave) gives more than 99% efficiency for the final optic. The residual light is scattered slightly because of minor surface roughness.

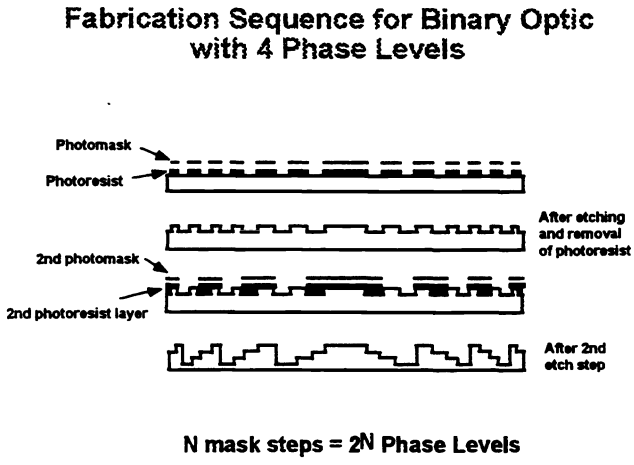

Figure 2 - Binary optic fabrication sequence for four phase level system. Most optics use four mask steps for sixteen phase levels.

There are several key variables that affect the design of a binary optic including: number of levels, lenslet $f^{\#}$, lens diameter, desired resolution, and substrate material and others. For the tomography applications it is desirable to have the number of lenslet elements be an integral power of two. Hence 32, 64, and 128 were the logical choices for the number of lenslets, although we also fabricated lenslet arrays of 40, 75 and 150 elements to verify the models. The lenslet diameter was chosen so that the overall array would be the same size as the detector (DALSA CL-C4-2048 pixels at 14μm pixel), or 28.67 mm. While this is a convenient means for choosing the lenslet size, it is by no means necessary. The arbitrary nature of the lenslet design is such that the lenslet array does not have to be the same size of the detector at all. Each lens element could be an off-axis portion of an overall lens, and hence the array could be made larger than the detector array in order to cover a larger field of view. This idea is explored in more detail in another paper[3]. The choice of overall diameter and number of lenslets along with the lenslet $f^{\#}$, completely specifies the array. For the 64 and 128 element designs an integral number of pixels per lens element is also possible.

The choice of lenslet focal length or $f^{\#}$ requires consideration of the diffraction pattern from a single lens, and of the diffractive coupling from one lenslet to another. The intensity pattern from a single cylindrical lenslet is given by the well known formula:

$$I(x)=I_0 \operatorname{sinc}^2\left(\frac{\pi x d}{f\lambda}\right)$$

which has minima at $x = \pm nf\lambda / d$. The spacing between adjacent lenslets, d, does not necessarily occur at an integral number of lobes on the sinc function. However, by choosing the appropriate focal length, the first (and subsequent) lobes can be made to either cancel or add. To make the nth lobe cancel, the spacing would need to be $d = nf\lambda / d$, with n even. With n odd, the lobes from adjacent lenslets add coherently. For Shack-Hartmann sensing, it is usually desirable to minimize the intensity between the focal spots. Thus a convenient design choice for lenslet focal length is:

$$f = \frac{d^2}{n\lambda}, \textit{ with n even}$$

In practice, however, it is not only the contribution from the first adjacent lens that effects the final intensity pattern. Since (for rectangular apertures) the lobe spacing is constant, there is a strong effect from several adjoining lens elements.

Table 1 gives a summary of five different lenslet designs. Once the basic lenslet parameters are specified (f, λ, d, N) then additional parameters may be calculated (spot size, number of pixels, lenslet sag, level discretization, etc.) These derived parameters are also shown in the spreadsheet in Table 1. Figure 3 illustrates the physical meaning of these parameters.

Table 1. Lenslet designs

	Symbol	40 Lens	64 Lens	128 Lens	75 Lens	150 Lens	Units	Formula
CAMERA								
Size of Camera Pixels	Wp	14.00	14.00	14.00	14.00	14.00	um	
Number of Pixels	Np	2048.00	2048.00	2048.00	2048.00	2048.00	pixels	
LENSLET ARRAY								
Operating Wavelength	Lambda	670.00	670.00	670.00	670.00	670.00	nm	
Index of Refraction	n	1.46	1.46	1.46	1.46	1.46		
Thickness	t	1.50	1.50	1.50	1.50	1.50	mm	
Length	L	25.40	28.67	28.67	28.67	28.67	mm	Np*Wp
Width	Wl	0.25	0.25	0.25	0.25	0.25	in	
Number of Lenslets	N	40.00	64.00	128.00	75.00	150.00		
Lenslets Per Inch	Ni	40.00	56.70	113.39	66.44	132.88		N*(25.4)/L
SINGLE LENSLET								
"Diameter"	d	635.00	448.00	224.00	382.29	191.15	um	L/N
F-Number	F#	157.48	83.60	83.60	98.00	98.00		
Focal Length	f	100.00	37.45	18.73	37.46	18.73	mm	F#*d
Sag	S	1095.72	1456.21	728.10	1060.04	530.02	nm	[(d/2)**2]/(2*R)
Sag in Waves		1.64	2.17	1.09	1.58	0.79	waves	S/Lambda
Radius of Curvature	R	46.00	17.23	8.61	17.23	8.62	mm	f*(n-1)
Number of Etched Levels	Ne	16.00	16.00	16.00	16.00	16.00		
Height of Etched Level	He	73.05	97.08	48.54	70.67	35.33	nm	S/(Ne-1)
Width of Narrowest Etching	We	10.77	7.60	3.80	6.48	3.24	um	(d/2)-sqrt(2*R*(S-He))
SPOT								
Pixels Per Lenslet	Nl	51.20	32.00	16.00	27.31	13.65	pixels	Np/N
Spot Half-Width	Hw	105.51	56.01	56.01	65.66	65.66	um	f*Lambda/d
Half-Width in Pixels		7.54	4.00	4.00	4.69	4.69	pixels	Hw/Wp
Spot Separation in Lobes	Nlobes	6.02	8.00	4.00	5.82	2.91	lobes	d/Hw
Dynamic Range	Theta_Max	3.58	5.98	5.98	5.10	5.10	mr	(Nl/2)*Wp/f
1/100 Pixel Resolution	Theta_100	1.40	3.74	7.48	3.74	7.47	ur	(0.01)*Wp/f

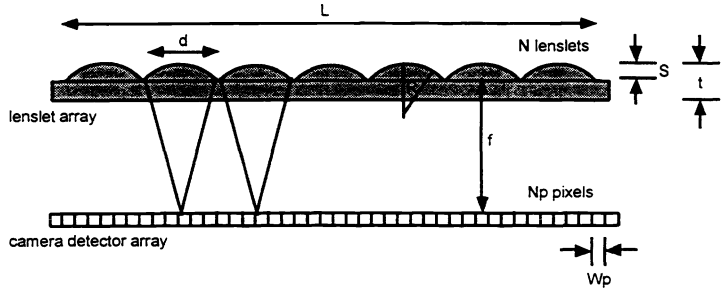

(a) SIDE VIEW OF LENSLET ARRAY AND DETECTOR ARRAY

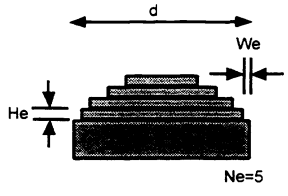

(b) LENSLET CROSS SECTION

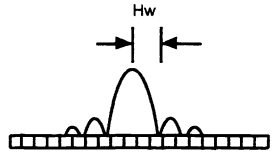

(c) SPOT INTENSITY CROSS SECTION

Figure 3 - Lenslet design parameters. Figure (a) and (b) are side views of the lenslets showing large and small scale features respectively. Figure (c) illustrates the spot intensity profile created by a lenslet.

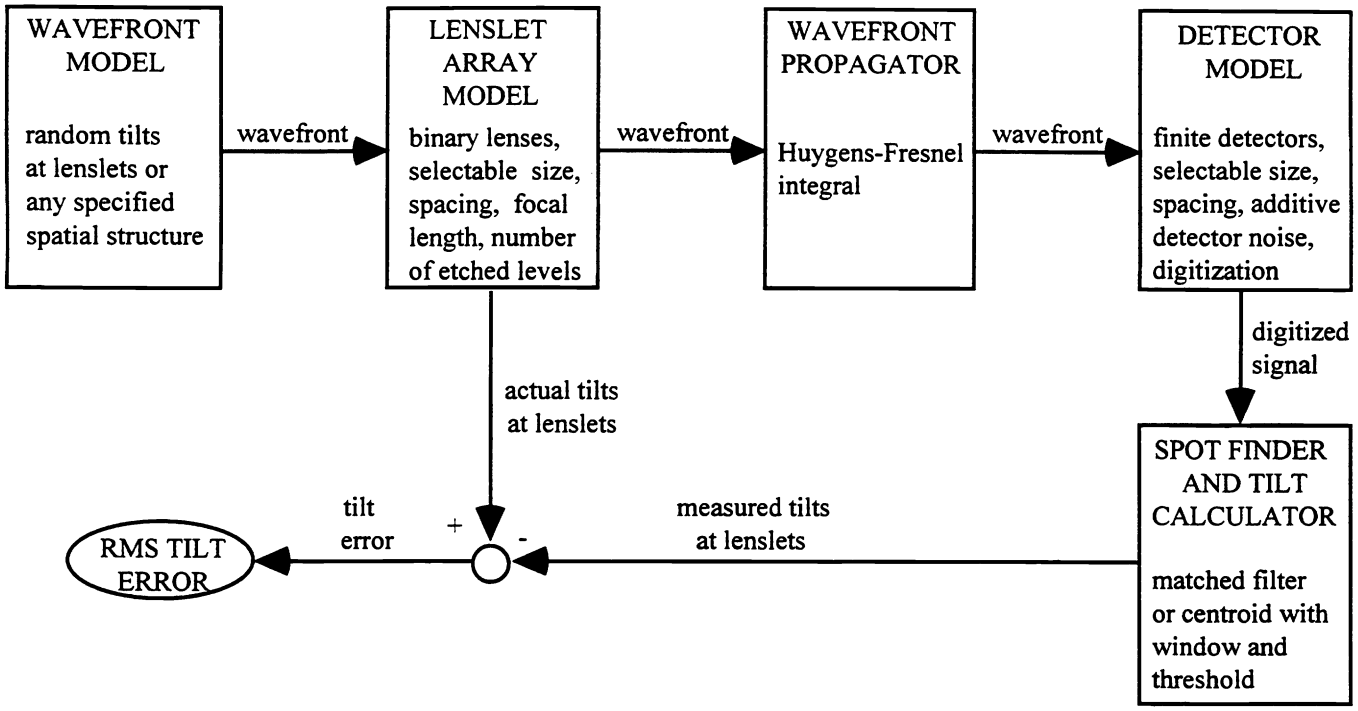

Figure 4 - Computer simulation for lenslet array performance prediction. The model allows evaluation of RMS tilt error due to such effects as coherent spot interference at the detector array

2.2 Performance Modeling

The performance of the wavefront sensor depends on relations between the lenslet array, the detector array, the wavefront to be measured, and the processing algorithm. Noise contributions arise from photon shot noise, detector noise, detector dynamic range and spatial extent, uncertainties in the physical layout, variations in lenslets and detectors, and interference between the spots. For a fixed detector array, these noise contributions result in a trade between sensitivity and dynamic range. Longer lenslet focal lengths increase sensitivity but limit dynamic range due to overlaps between neighboring Hartmann spots. Short focal lengths diminish sensitivity by focusing the power on only one or two noisy pixels, increasing spot location errors. In our case, the sensitivity requirement is high while the dynamic range is very small; therefore the "best" design shows considerable coherent interaction between Hartmann spots. The situation is further complicated by a dependence on the nature of the wavefront being sensed, because the structure of the wavefront determines the degree of interference between wavefront sensor spots.

We constructed a computer model of the one dimensional Hartmann Sensor that predicts wavefront sensor performance under realistic conditions. Figure 4 summarizes the modeling process. The model propagates simulated wavefronts through a lenslet array to a detector, calculates intensity at each pixel, and adds detector noise to the resulting signal. These simulated spot profiles are processed by the same spot location codes used for laboratory data, and the resulting tilt measurements are compared with the true tilts at each lenslet in the simulated wavefront.

The simulation allows investigations over a wide parameter space. For example, the wavefronts are arbitrary complex fields which may contain coherent structures much larger or

smaller than the lenslets. The lenslet array contains any number of cylindrical lenses at any spacing, and each lens is a binary optic with a specified number of etched levels. The focal length of the lenses and distance from lenslet array to the detector are independent variables; this flexibility enables investigations of performance away from focus. The number of detectors, spacing, size, and detector noise are controllable to match the physical system, and intensity is integrated over the detector. The simulation performs Huygens-Fresnel propagation from the lenslets to the detector array, thus avoiding far-field assumptions. Broad band illumination may be modeled by summing detected intensities for propagated fields at a number of wavelengths across the band.

Because of its generality, the model for coherent illumination requires considerable CPU time on our SUN Sparc-2CE workstation. Therefore, we also use a simplified computer model restricted to incoherent illumination, perfect spherical lenslets, and detectors located at the lenslet focal plane.

Figure 5 illustrates simulation results as a function of the number of discrete levels etched on each lenslet. In plot (a) the profile of a lenslet with 8 etched levels is compared with an ideal spherical profile. In plot (b), the resulting spot intensity and phase profiles at the nominal focus are compared for a spherical lenslet and two binary lenslets with 8 and 4 etched levels. As might be expected, reducing the number of etched levels diminishes the match to a spherical surface and spoils the lenslet focus; this change exhibits itself primarily in an alteration of the spot phase profile. If there are only a few etched levels, the intensity profile is also altered, and some power is shifted from the central spot to outlying lobes. This shift of power increases interference between neighboring spots and diminishes sensor performance. However, a lenslet with only 8 etched levels produces a profile remarkably close to the ideal spot. Our design, at 16 etched levels, shows essentially identical performance to the spherical lenslet.

The model has also verified some design criteria which had previously been deduced empirically. For example, the principle used in section 2.1 to select lenslet focal length attempts to space wavefront sensor spots such that their side lobes cancel. This implies that sensor performance should be a periodic function of spot overlap, good at certain spot spacings and worse at others. The modeled performance in figure 6 shows just this type of periodic behavior.

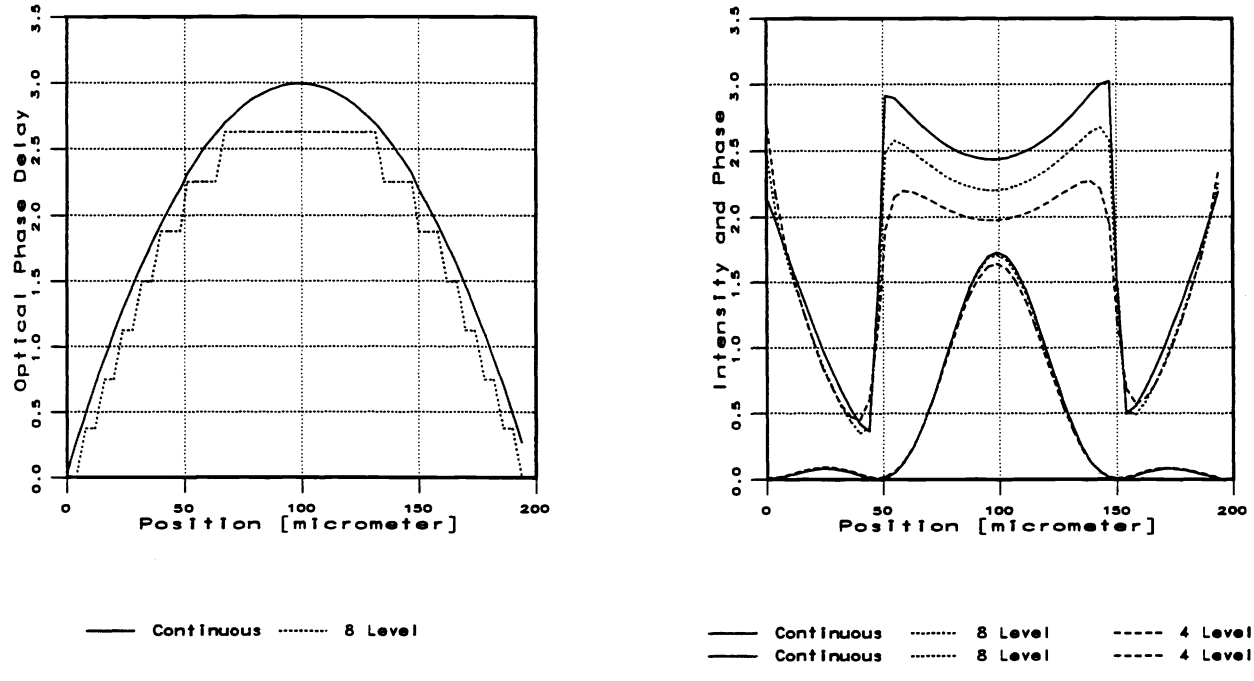

Figure 5 - Binary lenslet simulation. (a) profile of 8 level binary lenslet compared to ideal spherical surface (b) spot intensity profiles and phase for 4 level, 8 level, and ideal lenslet

Figure 6 is a design curve which plots predicted measurement error versus focal length. This particular design curve is for a one inch long 40 element lenslet array and a 2048 element detector array with 14 micron pixels. The three curves represent sucessive addition of measurement noise sources.

The lowest curve indicates high light level performance for a single lenslet with no detector noise. Without neighboring spots, the measured tilt error is essentially constant and limited by processing error or quantization noise. At extremely short focal lengths the sensor fails, since the spot collapses to a single pixel and cannot be accurately located.

The middle curve indicates performance for the full lenslet array, allowing interaction between the spots. At longer focal lengths, the spot size grows, and the interference between adjacent spots increases. The periodicity is due to successive overlap of spot side lobes between spots.

The top curve adds realistic detector noise to the simulation of the lenslet array. This additional noise source mutes the periodic structure of the performance curve and pushes the optimum performance point to a slightly longer focal length.

It should be noted that Figure 6 represents incoherent addition of adjoining spots; simulations with coherent illumination show much more complex behavior at finer scales due to interference from several neighboring spots. Section 3.1 provides an example of this behavior.

3. WAVEFRONT SENSOR CHARACTERIZATION

To evaluate the laboratory performance of wavefront sensors and compare it to the predicted performance from our computer model, we set up a test system as depicted in Figure 7. This test system is designed to allow controllable changes in both wavefront and lenslet position. At the nominal lens positions, we produce flat wavefronts are for sensor reference and sensor noise tests. By repositioning the lens L_2, the lens relay also allows introduction of wavefronts of known curvature. In addition, the detector array position may be accurately adjusted to lie at the focal plane of the lenslet array or on either side of the focal plane.

The majority of tests described in this section are short term noise tests. During these tests, the input wavefront is a flat reference beam, and data is collected over a short time period, usually a fraction of a second. For each lenslet, we calculate a self-referenced spot position by averaging spot positions over the sampling period. We then calculate the RMS tilt error as the RMS of all measurements against the self-reference.

Long term tests over periods of several hours are also performed, however, the results are more complex due to gradual changes in the reference wavefront and other sources of error. We hope to discuss these results in a later publication.

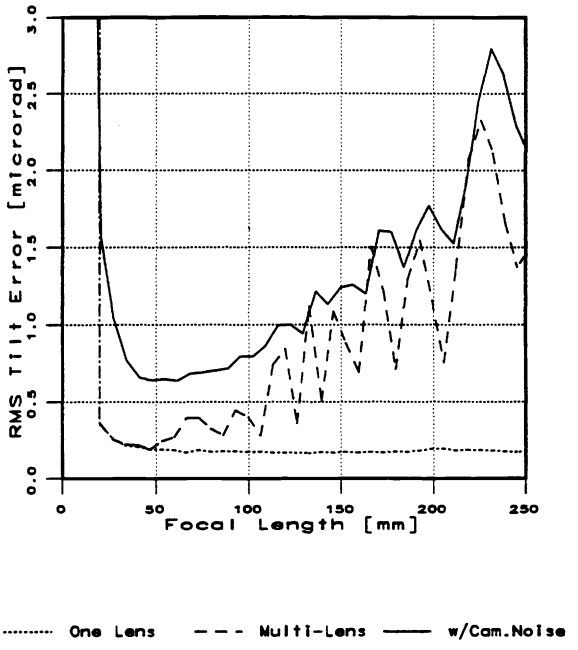

Figure 6 - Predicted performance as a function of focal length. The periodicity is due to interference between side lobes of the Hartmann spots.

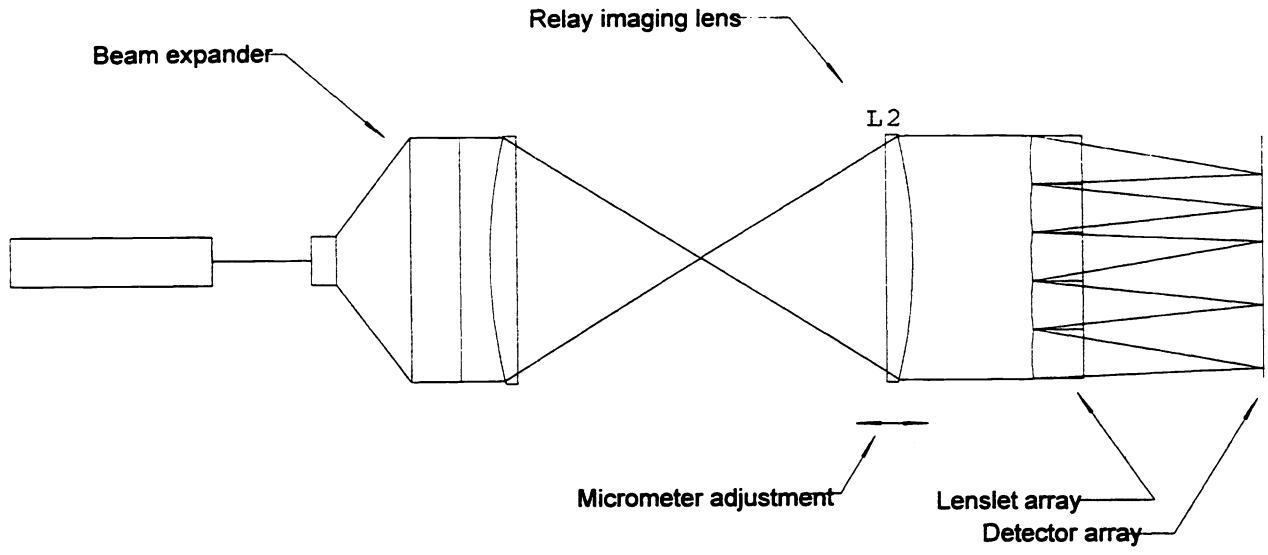

Figure 7 - Laboratory wavefront sensor test configuration. The movable lens L_2 allowed injection of a spherical wavefront into the system.

3.1 Comparison of predicted vs. observed performance

To check the basic model assumptions, we compared the predicted and observed intensity profiles of individual Hartmann sensor spots for the various lenslets. Figure 8 is an example for the 64 lenslet design described in Table 1. The solid curve shows the observed intensity profile over a central portion of the array for a flat reference wavefront. The dotted curve shows the predicted intensity profile obtained by modeling a flat incident wavefront where the power incident at each lenslet has been normalized to match the measured data. Note that the structure of the predicted and measured spots agrees well in lobe spacing and structure between the spots, but the measured spots have an intensity distribution skewed to the right. The presence and direction of skew is variable, often indicating poor alignment of the sensor and the illumination. It indicates undesirable structure in the reference wavefront over each lenslet, but does not preclude wavefront sensor operation. We have obtained good performance even with distorted spots.

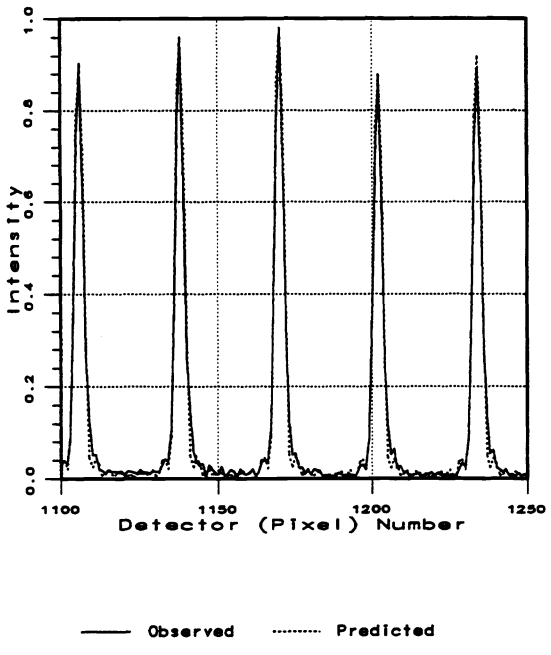

Figure 8 - Predicted and observed Hartmann spot intensity profiles. Model and measurement show good agreement; however measured spots are often skewed.

We have run both simulation and laboratory performance tests for wavefront sensors using the lenslet designs described in Table 1. For short term measurement, model and experiment show good agreement. Figure 9 plots curves of predicted RMS tilt error versus focal length for the 40, 64, and 128 element lenslet arrays. Each curve is calculated for incoherent illumination and shows a performance tradeoff between short focal lengths, which reduce spot interference, and longer focal lengths, which mitigate detector noise. The two sets of X marks on the plot indicate the measured operation points of the 40 and 64 element wavefront sensors under coherent illumination. The 64 element sensor was designed to operate near the optimum performance point on the performance curve, and its performance agrees well with the prediction. The 40 element sensor exceeds predicted performance, falling slightly below the plotted curve.

Figure 10 plots the same 40 lenslet performance data but adds an additional performance prediction curve for coherent illumination. The measured performance for the 40 lenslet sensor under coherent illumination does agree with the predicted performance and seems to be near a global minimum. However, the performance of the wavefront sensor under coherent simulation is much more finely structured as a function of focal length than the corresponding curve for incoherent illumination. This high sensitivity to small changes in optical design or experiment layout seems to be characteristic of wavefront sensor performance in the coherent case, and we are still investigating its implications.

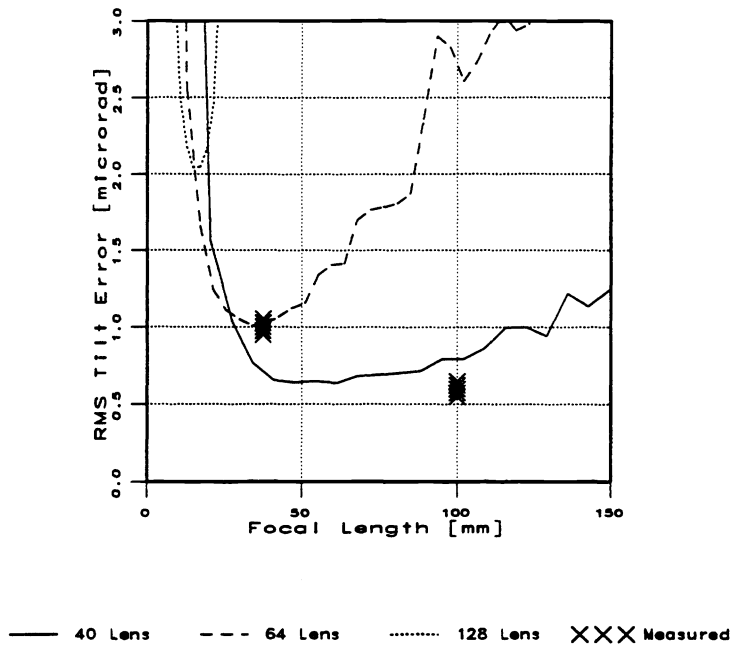

Figure 9 - Predicted and observed tilt error. Predicted performance is shown for 40, 64, and 128 lenslet designs. Actual measurements are marked for 40 and 64 lenslet designs.

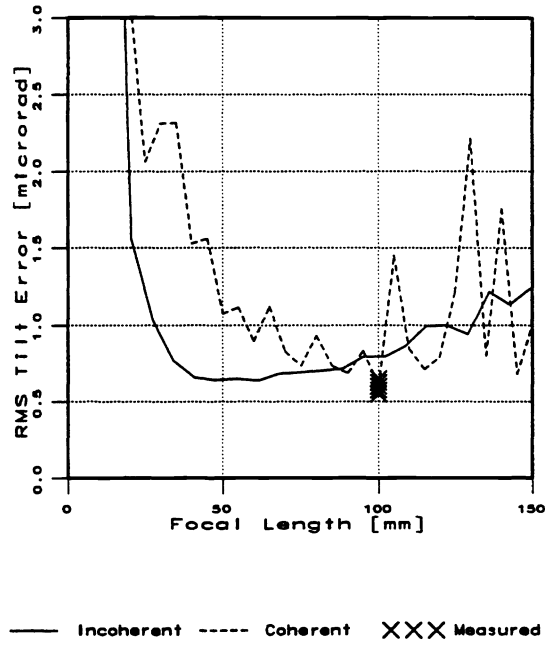

Figure 10 - Coherent vs. incoherent illumination. The predicted performance for the 40 lenslet array design indicates complex behavior under coherent illumination.

In addition to problems associated with coherent plane wave illumination, we are also investigating the behavior of the wavefront sensor when exposed to strong wavefront structure. By strong wavefront structure, we mean any wavefront, such as curvature, which causes tilt to vary deterministically from lenslet to lenslet across the array. Figure 11 illustrates one experiment using wavefront curvature. In this experiment, the curvature of the wavefront was changed by moving lens L2 in the laboratory test system (see Figure 7). Pure curvature is sensed by the wavefront sensor as a linearly increasing tilt across the lenslet array. For an ideal wavefront sensor, the presence of curvature would not alter the apparent error. Neither the spatial RMS nor the temporal RMS should increase once the linear trend is removed, and the RMS error curve in Figure 11 would be a horizontal line. However, as Figure 11 shows, the apparent error does increase with increasing curvature.

Both data and simulations confirm the existence of this accumulating error. It is due to the structured of the curved wavefront which leads to a deterministic interaction among Hartmann spot side lobes.

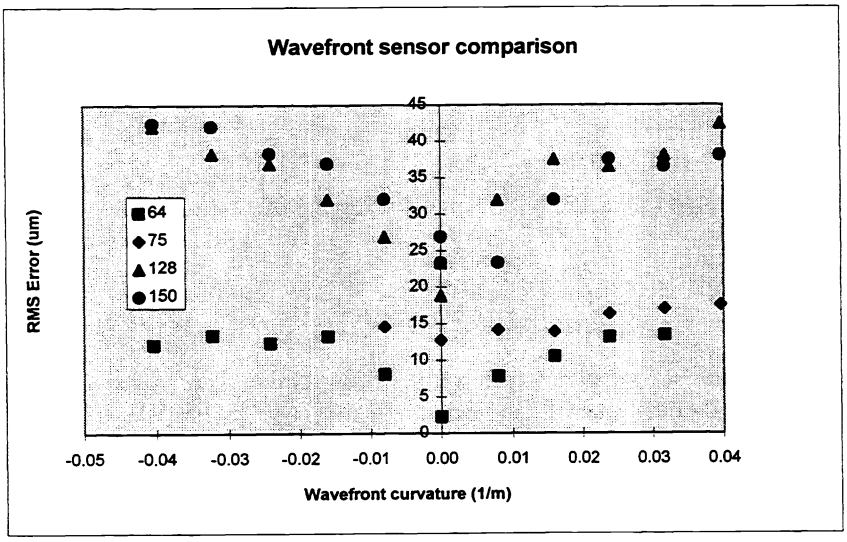

Figure 11 - Error as a function of wavefront curvature. The plot shows performance for the 64, 75, 128, and 150 lenslet arrays and confirms that measurement error is not independent of wavefront structure.

4. TOMOGRAPHY SYSTEM

4.1 Tomographic Performance Prediction Method

Performance of the wavefront sensor is only one contributor to tomographic imaging performance. The number of tomographic views, configuration of these views, and structure of the flow to be imaged also contribute strongly to system performance.

In order to investigate alternate tomographic system designs and predict expected performance, we developed a computer model of the system configuration and tomographic reconstruction process. The model projects through a two dimensional image of the flow field, adds noise to the projections, back projects to form a recovered flow field, and compares the recovered flow field to the truth. Figure 12 indicates the main features of the tomographic model. Since the quality of the recovery is highly dependent on the size of the features being imaged, the model employs a metric that predicts system performance as a function of spatial frequency in the flow field.

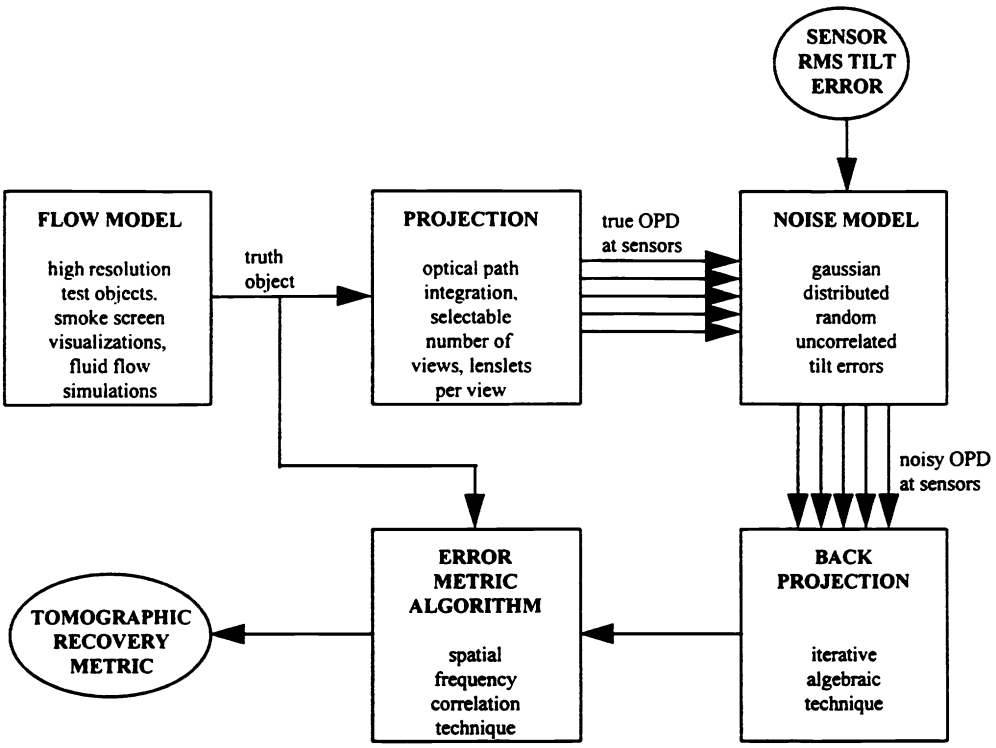

Figure 12 - Computer simulation for tomographic performance prediction. The model uses known flow structure and known wavefront sensor tilt errors to predict reconstruction quality.

Since the structure of the flow field is known to influence the quality of the recovery, it is important to select flow models that realistically represent expected conditions. However, data at the required spatial and temporal resolution is scarce. Therefore we fuse data from a number of sources including fluid flow simulations, high temporal bandwidth measurements from single quad-cells or wavefront sensors, and low temporal but high spatial resolution images captured by entraining smoke in the jet and illuminating one horizontal sheet in the flow. We refer to these latter images as "flow visualizations" and expect that they reflect the type and scale of structure was present in the flow.

The noise added to each projection through the model flow is based on the predicted wavefront sensor error obtained from the model described in section 2.2 or based on measured wavefront sensor errors described in section 3. In either case the noise from detector to detector is assumed to be gaussian distributed and uncorrelated between lenslets and between wavefront sensors. This assumption is poor when measuring strong structures in the flow (as demonstrated, for example, by the data in Figure 10) but is probably adequate for the weak disturbance expected in our flow measurement system.

4.2 Performance Prediction Results

An 8 view tomographic imaging system is nearing completion at the Phillips Laboratory. Each view is a 64 element one-dimensional wavefront sensor arranged in a half circle around the flow to be imaged. Using the tomographic system simulations described in the previous section, we have modeled the performance of this 8 view system under expected noise conditions for the 64 lenslet wavefront sensor.

Figure 13 shows one example of expected recovery quality for reconstruction of a flow field. The gray scale images represent air density within a two dimensional horizontal slice through the flow. Image (a) is the truth model at high resolution; it was formed from a flow visualization at 1.5 nozzle diameters downstream from the nozzle. Image (b) is the recovered image with

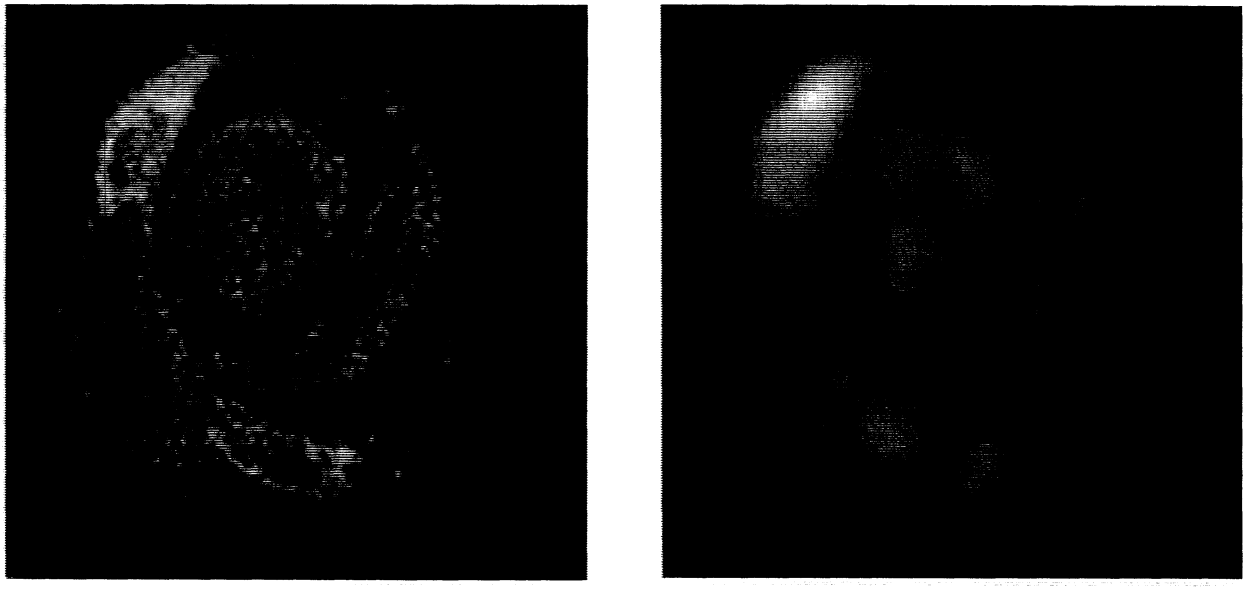

Figure 13 - Expected flow field recovery quality. Figure (a) is the truth model based on a smoke visualization of an actual flow field. Figure (b) is the recovered flow field based on 8 views 64 lenslets per view and predicted wavefront sensor noise.

resolution limited both by finite sampling and wavefront sensor noise.

Figure 14 summarizes the image content of the recovered flow field as a function of spatial frequency for the same simulation shown in Figure 13. The metric indicates the degree of correlation between structures in the recovered flow field and structures in the truth image. The plot indicates high correlation and good recovery quality out to 0.14 cycles/mm and little information beyond 0.30 cycles/mm. Converting from spatial frequency to corresponding feature sizes, we find that features of 3.5 mm and larger were recovered by the tomographic system, but all features less than 1.6 mm in size were lost.

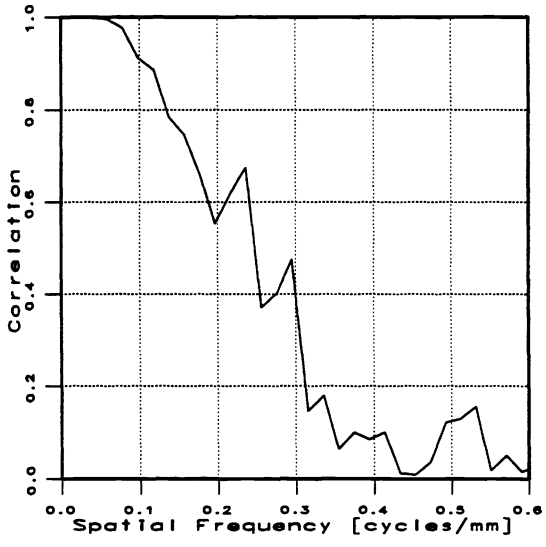

Figure 14 - Recovery quality. The correlation metric indicates the degree of model flow field recovery as a function of spatial frequency.

5. CONCLUSIONS

A tomographic imaging system is nearing completion which provides time resolved images of heated air flows. The system is comprised of a semicircle of Hartmann wavefront sensors with intersecting views through the flow. Linear CCD arrays combined with arrays of cylindrical lenslets allow flow sampling at rates up to several kilohertz, and performance is limited by measurement errors in the wavefront tilt measurements. We have developed designs for one dimensional lenslet arrays based on binary optics, fabricated these binary lenslet arrays, and demonstrated their performance in the laboratory. We have also developed computer models of the wavefront sensors and shown agreement of modeled results with laboratory measurements. Over short time periods, tilt errors are on the order of a microradian, limited primarily by detector electronic noise. By introducing this wavefront measurement error into a computer simulation of the tomographic system, we can evaluate the quality of expected flow reconstructions. The eight view system under construction in the laboratory is expected to resolve flow features down to three millimeters.

---

[1] L. McMackin, B. Masson, K. Bishop, R. Pierson and E. Chen, "Hartmann wavefront sensor studies of dynamic organized structure in flow fields," to be published in the AIAA Journal.

[2] D. R. Neal, T. J. O'Hern, J. R. Torczynski, M. E. Warren and R. Shul, "Wavefront sensors for optical diagnostics in fluid mechanics: application to heated flow, turbulence and droplet evaporation," SPI Vol. 2005, pp. 194-203 (1993).

[3] D.R. Neal, J.D. Mansell, J.K. Gruetzner, R. Morgan, and M.E. Warren, "Specialized wavefront sensors for adaptive optics," SPIE 2534-32 (1995).